



Synthesis of graphene-based photocatalysts for water splitting by laser-induced doping with ionic liquids

Angel Pérez del Pino ^{a,*}, Arántzazu González-Campo ^a, Sandra Giraldo ^{a,b}, José Peral ^c, Enikő György ^{a,d}, Constantin Logofatu ^e, Andrew J. deMello ^f, Josep Puigmartí-Luis ^{f,**}

^a Instituto de Ciencia de Materiales de Barcelona, Consejo Superior de Investigaciones Científicas (ICMAB-CSIC), Campus UAB, 08193 Bellaterra, Spain

^b Departament de Farmacologia i Química Terapèutica, Universitat de Barcelona, Av. Joan XXIII, 08028, Barcelona, Spain

^c Departament de Química, Universitat Autònoma de Barcelona, 08193 Bellaterra, Spain

^d National Institute for Lasers, Plasma and Radiation Physics, PO Box MG 36, 77125 Bucharest, Romania

^e National Institute for Materials Physics, PO Box MG 7, 77125 Bucharest, Romania

^f Institute of Chemical and Bioengineering, Department of Chemistry and Applied Biosciences, ETH Zurich, Switzerland

ARTICLE INFO

Article history:

Received 18 August 2017

Received in revised form

21 December 2017

Accepted 28 December 2017

Available online 2 January 2018

ABSTRACT

The synthesis of metal-free graphene-based photocatalysts has received great attention recently due to their expected contributions to the development of solar-based hydrogen generation via water-splitting in a low cost and ecological manner. In this work, a new method for the generation of nitrogen-doped graphene-based powder employing an alternative solution to commonly used toxic and hazardous organic solvents is presented. The procedure involves ultraviolet pulsed laser irradiation of graphene oxide (GO) flakes dispersed in 1-butyl-3-methylimidazolium [bmim]-based ionic liquids using both chloride and acetate anions. The structural and compositional analysis using transmission electron microscopy, X-ray photoelectron and infrared spectroscopy indicate that the irradiated GO becomes partially reduced and doped with graphitic, pyrrolic and pyridinic nitrogen species. Interestingly, the relative content of the nitrogen functionalities is controlled by the anion in the ionic liquid and its concentration, with the obtained graphene-based powders showing higher photocatalytic activity than GO. Furthermore, a remarkable synergistic effect is observed for GO-[bmim]-acetate powder (acting as co-catalyst) in combination with anatase TiO₂ nanoparticles. The presented method opens new research avenues for the cost-effective mass production of graphene-based photocatalysts for water splitting applications.

© 2018 Elsevier Ltd. All rights reserved.

1. Introduction

The massive and ever growing amount of energy consumed by mankind (currently based on fossil fuels) is causing unprecedented damage to the biosphere. Accordingly, the substitution of conventional energy sources by renewable-based technologies is imperative. One of the most promising renewable alternatives involves the use of hydrogen as a fuel, since hydrogen can be produced from renewable resources and can be safely stored [1]. A promising strategy for converting solar energy into clean and carbon-free H₂ fuel at low-moderate cost and in an environmentally neutral

manner involves the photoinduced splitting of water into hydrogen and oxygen using semiconductor-based photocatalysts [2]. Significantly, the main problem associated with H₂ generation from water is achieving water oxidation with photogenerated holes. However, using organic compounds, whose oxidation is thermodynamically more favourable than water, impedes electron-hole recombination in the semiconductor and, therefore, the reduction process (H₂ generation) is favoured. The overall process of heterogeneous photocatalytic H₂ generation through the consumption of organic compounds can be also interpreted as photoinduced biomass reforming or photoreforming [3,4].

A large number of semiconductor photocatalysts have been investigated [2]. TiO₂ is one of the most extensively investigated due to its low cost, abundance, chemical stability, and minimal toxicity [5]. At present, most established photocatalyst systems use noble-metal-based co-catalysts, mainly Ru, Rh, Pd, Pt, Au and Ag, to

* Corresponding author.

** Corresponding author.

E-mail addresses: aperez@icmab.es (A. Pérez del Pino), josep.puigmarti@chem.ethz.ch (J. Puigmartí-Luis).

ensure high photocatalytic performance [6]. Such photocatalysts can be used either in a powdered or electrode-coated form [3,7,8]. In this respect, it is important to note that the varying availability of many important chemical elements poses major challenges for the widespread implantation of renewable technologies, including photocatalytic-based ones. Accordingly, substitute materials are required [9]. An attractive alternative to transition metals and rare-earths are metal-free carbon nanomaterials, which show unique properties, including high electrical conductivity, large surface area and tunable morphologies. In addition, they can be generated in abundant quantities and via cheap, robust and non-toxic routes. In this context, graphene-based materials have recently been of particular interest as they exhibit extraordinary physico-chemical properties as photo- and co-catalysts [10]. Significantly, their excellent mechanical, thermal and electrical properties, in addition to their large surface area, make graphene-based materials ideal candidates for the development of relatively low-cost and high performance photocatalysts [11]. However, new carbon-based derivative materials together with advanced synthetic pathways that require non-hazardous processing technologies (e.g. avoiding the use of toxic organic solvents) are still required to ensure further improvements in water splitting. In particular, graphene oxide (GO) materials, which are composed of graphene sheets bonded to oxygen-containing chemical groups, have become popular in water-splitting applications due to their rich chemistry and derivatization possibilities [12]. GO sheets can be reduced by chemical routes at high temperatures, leading to a material that resembles pristine graphene, so called reduced GO (rGO). More recently, laser irradiation of GO nanosheets in different environments has allowed their photoreduction [13–16] and doping [17–21]. Indeed, GO can adapt an extended conformation in aqueous solution, which makes it an effective medium for photocatalytic water-splitting without the need for noble metal co-catalysts [11,22]. Finally, GO exhibits p-type conductivity, leading to the creation of an accumulation layer at the GO/water interface, which favours water reduction to hydrogen [23].

The replacement of functional oxygen groups on the GO sheet edge with nitrogen-containing chemical groups transforms GO into an n-type semiconductor [23,24]. Indeed, the direct substitution of carbon atoms with nitrogen in the graphene lattice induces the modulation of optical and electronic properties [25]. Since nitrogen-containing GO exhibits n-type characteristics, it assists the promotion of hole transfer for water oxidation to oxygen [22]. Thus, modification of graphene sheets to exhibit both p- and n-type properties may produce a photocatalytic medium that is effective for overall water-decomposition into H_2 and O_2 [26] with improved efficiency at visible wavelengths. The high conductivity of graphene domains in rGO additionally enhances the effective exciton separation and charge transfer processes essential for overall water-splitting. Accordingly, metal-free graphene-based photocatalysts are likely to make solar-based hydrogen generation from water-splitting achievable at low cost and in an environmentally-friendly manner. To date, the synthesis of photocatalysts is typically achieved using solution-based methods [27]. Although these techniques possess attractive features, they are not bereft of disadvantages, such as chemical incompatibilities, problems in synthesizing multicomponent materials and the need for complex multi-step processes, which means the presence of toxic chemical substances and high temperatures for several hours. Recently, it has been demonstrated that laser irradiation of GO sheets dispersed in an ammonia-rich liquid medium arises as an effective strategy for the introduction of nitrogen-based heteroatoms into the rGO structure [28]. However, ammonia is a corrosive and toxic chemical, and therefore, the quest for an environmentally friendly and non-toxic process enabling an efficient and controllable nitrogen doping of GO is of valuable

importance for further developments in the field. Interestingly, this technique could account for a facile, high-throughput and versatile method for the synthesis of graphene-based photocatalyst powders for production of solar hydrogen.

In this contribution, we report an envirometally friendly and non-toxic synthesis of photoactive N-doped rGO photocatalyst powders via laser irradiation of GO sheets immersed in nitrogen-containing ionic liquids (ILs). ILs are low temperature molten salts, and hence, are non-volatile liquids composed entirely of ions below or around room-temperature [29]. ILs are commonly referred to as designer solvents; that is, in contrast to conventional solvents their composition can be adjusted to dictate reactions and reagents solubility. For example, their hydrophilicity or hydrophobicity can be adjusted by judicious choice of the organic cation and the identity of the anion employed during synthesis [30]. Their ionic behaviour has been used to influence crystallization processes [31], and furthermore, their wide electrochemical window has enabled the electrodeposition of materials that could not be deposited from common aqueous or organic solvents [32]. However, in all such cases ILs are employed as enviromentally friendly solvents for materials engineering. In this work, we aim to go one step further and use ILs simultaneously as both solvents and reagents for the functionalization of GO through laser-induced chemical routes. To the best of our knowledge, this concept has yet to be addressed since IL doping of GO has hitherto been done through usual chemical routes [33–35]. We have chosen two imidazolium-based ILs with different anions, 1-butyl-3-methylimidazolium chloride ([bmim]Cl) and 1-butyl-3-methylimidazolium acetate ([bmim]Ac). It has been reported that the identity of the anion can strongly influence properties such as hygroscopicity, surface tension or hydrogen-bonding ability [30,36]; parameters that are likely to motivate different functionalization of GO.

2. Experimental

1-Butyl-3-methylimidazolium chloride ([bmim]Cl) and 1-butyl-3-methylimidazolium acetate ([bmim]Ac) were purchased from Sigma-Aldrich and used as received. Aqueous solutions (ca. 40 wt.%) of [bmim]Cl ($\geq 99.0\%$) and [bmim]Ac ($\geq 95\%$) were prepared in water (hereafter termed as IL-Cl and IL-Ac, respectively). The as-prepared solutions were then stirred at room temperature for 30 min before use. Next, GO powder (NanoInnova Technologies) was dispersed in IL-Cl and IL-Ac to obtain solutions of 1 wt.% GO. After thorough stirring and sonication, the resulting GO-ILs dispersions were then placed in quartz cuvettes. The dispersions were stable for few tens of hours.

Laser irradiation experiments were performed using a Nd:YAG laser (Brilliant B, Quantel) emitting 5 ns laser pulses at 266 nm and at a repetition rate of 10 Hz. The laser energy was set to 100 mJ, the spot dimensions were ca. 64 mm² and an accumulation of 4000 pulses per gram of dispersion was applied to the solutions, under constant stirring (Fig. 1). Subsequently, the final mixtures (denoted as GO-IL-Cl and GO-IL-Ac) were centrifuged to separate the functionalized GO sheets from the ionic liquids, with the resulting solid then being washed with MilliQ water four times to remove physisorbed IL. Each cleaning step involved the addition of MilliQ water and centrifugation for 20 min at 2000 rpm. For GO-IL-Cl an extra cleaning step was necessary to isolate the final solid. Water was removed by centrifugation at 900 rpm for 4 h, and samples dried at 60 °C. Finally, a control sample composed of 1 wt.% GO aqueous dispersion without any ionic liquid (GO-H₂O) was synthesized following the method used for the preparation of the other samples.

The obtained powder was characterized by high resolution transmission electron microscopy (HRTEM) and selected area electron diffraction (SAED) using a FEI Tecnai G2 F20 microscope

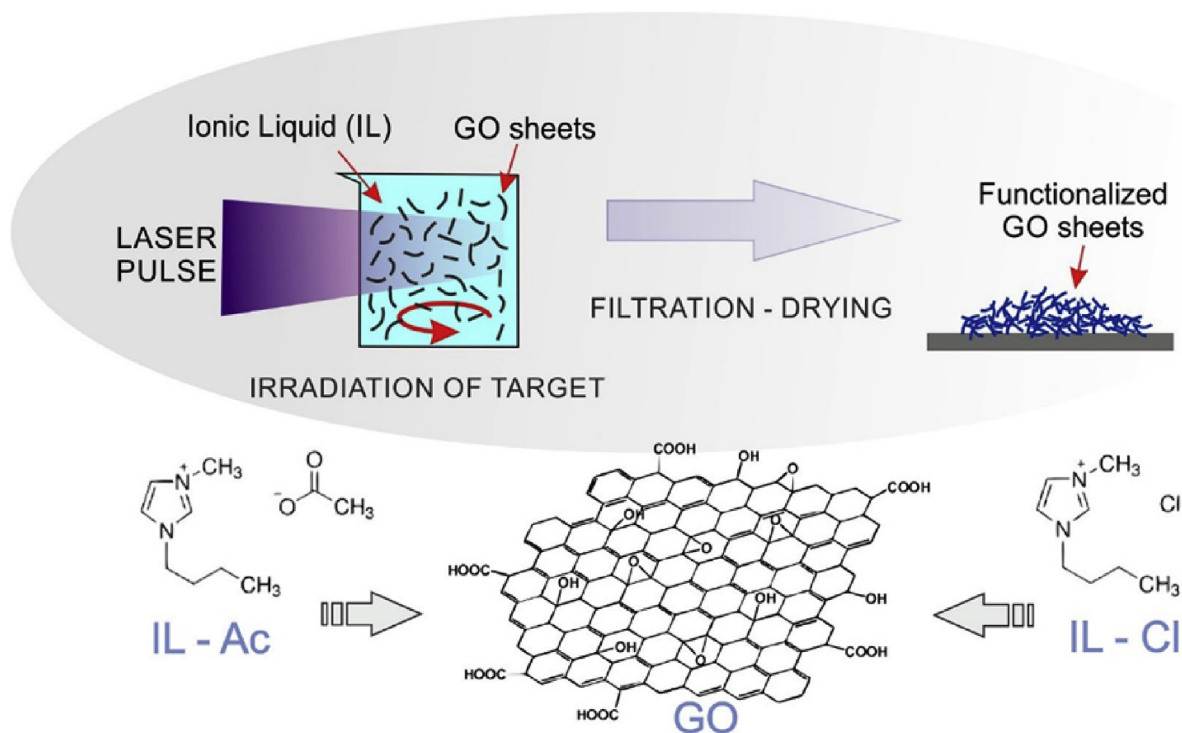


Fig. 1. Summary of the laser irradiation experiments. GO sheets dispersed in an IL solution are irradiated with UV radiation, filtered and dried to obtain functionalized GO powder. The molecular structures of the two types of ILs used, [bmim]Cl (IL-Cl) and [bmim]Ac (IL-Ac), are also presented. (A colour version of this figure can be viewed online.)

operating at 200 kV. Material composition was characterized by attenuated total reflectance Fourier transform infrared spectroscopy (ATR-FTIR) using a Perkin-Elmer Spectrum One spectrometer. Raman spectroscopy measurements were carried out through a Horiba Jobin Yvon LabRAM 800 equipment. Several spectra were acquired in the 400–2000 cm^{-1} range using 1 mW laser radiation (532 nm wavelength) focused in spots of 0.5–1 μm in diameter. An average of 3 spectra with 20 s of acquisition time was recorded for improving the noise to signal ratio. X-ray photoelectron spectroscopy (XPS) studies were also performed on a SPECS XPS spectrometer, based on a Phoibos 150 electron energy analyser, operating in constant energy mode. The XPS spectrometer used a monochromatic X-ray emitter of AlMg K α (1486.74 eV). Full spectra were acquired using an analyzer pass energy of 50 eV, whereas high resolution spectra were acquired over smaller ranges (20 eV) at 10 eV pass energy with an energy resolution of 0.6 eV (Ag 3d5/2 line FWHM). All analyses were performed in ultra-high vacuum ($\sim 10^{-7}$ Pa). Chemical analysis of the ILs was carried out using nuclear magnetic resonance prior to and after laser processing to assess possible chemical variations in structure. For these experiments, a Bruker Avance II 300 system equipped with a QNP-z (1H/13C/19F/31P) probe was used. The ^1H NMR spectra of the ILs were performed in D_2O . Photocatalytic properties and hydrogen generation capability of the obtained powders were assessed using water–methanol solutions (photoreforming). The main element of this experimental set up was a double wall cylindrical Pyrex reactor of 125 mL volume, fitted with a gas inlet and outlet, connected to a thermostatic bath, and placed on a magnetic stirrer. Four lamps (15 W compact UVA lamps) surrounding the reactor provided UVA-light radiation. In all experiments, 80 mg of catalyst was added to 50 mL of an aqueous solution of methanol (0.005 M or 0.25 M concentrations). The reactor was then closed and remaining air (~ 75 mL) pumped out and replaced with pure N_2 . Subsequently, the lamps were turned on and the solution irradiated. Hydrogen

evolution was assessed using gas chromatography with a Shimadzu GC-2014 chromatograph equipped with a packed column (Carboxen 1000 stationary phase) and a TCD detector. Injections were performed using a six port injection valve with a fixed 2 mL volume loop. Reinecke's salt actinometry [37] was performed to quantify the number of photons entering the reactor when using the four UVA lamps ($5.3 \times 10^{-7} \text{ E s}^{-1}$). The incident power at the outer reactor surface was calculated taking into consideration the lamp spectrum and the hypothetical lamp power output. The assumed lamp power is changed in the spreadsheet until the calculated number of photons matches the actinometry outcome. In this way, and considering the reactor geometry, it was possible to estimate an incident irradiance of $3.1 \times 10^{-3} \text{ W cm}^{-2}$. Actinometry allowed the assessment of the photonic efficiency (ϕ), given by:

$$\phi = \frac{2 \cdot \text{Number of } \text{H}_2 \text{ molecules produced}}{\text{Number of incident photons}} \cdot 100 \quad (1)$$

3. Results and discussion

The morphology and crystallinity of raw GO (reference, Ref GO) and laser processed GO-IL-Ac and GO-IL-Cl powder were investigated extensively using TEM (Fig. 2). The reference GO powder is composed of multi-layered (4–15 layers) platelets, between 400 nm and 1 μm in size, exhibiting flat surfaces with no folds or remarkable structural defects, see also Supporting Material Fig. S1. TEM selected area electron diffraction (SAED) images recorded in regions approximately 100 nm in size reveal the characteristic 6-fold hexagonal pattern of a sp^2 graphene lattice (spots at $1/d$, where $d = 0.14, 0.25 \text{ nm}$), although the spots are slightly extended along circular geometry (Fig. 2a inset). This pattern is characteristic of a polycrystalline lattice with preferred orientation. The

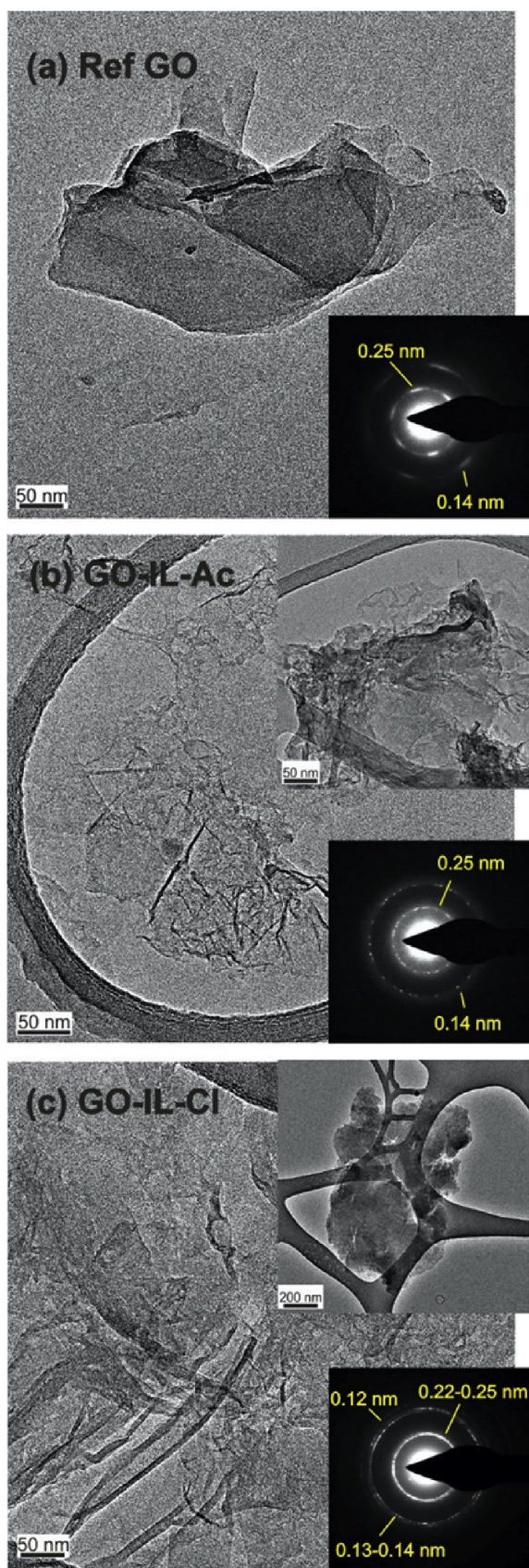


Fig. 2. TEM images and corresponding SAED patterns of (a) raw GO (reference), (b) GO-IL-Ac and (c) GO-IL-Cl platelets. (A colour version of this figure can be viewed online.)

stretching of the spots would have a double origin: (i) the GO platelets can be turbostratic multilayers in nature; (ii) the underlying structure of the monolayer regions is nanocrystalline (sp^2 domains surrounded by oxygen-bonded sp^3 ones), therefore the graphitic structure of each crystal is independently rotated with respect to each other. As a consequence, intra- and interlayer rotation between crystallites results in circular SAED patterns, similar to those of polycrystalline materials [38]. Microscopically, GO-IL-Ac (Fig. 2b) platelets have similar dimensions than non irradiated ones though appear rather wrinkled and exhibit zones containing nanometer-sized holes. The observed wrinkles are a few nanometers wide, but can extent to more than 100 nm in length. Electron diffraction reveals ring patterns decorated with multiple spots, characteristic of polycrystalline materials. The rings appear more diffuse than those associated with the raw GO reference, especially in regions with high concentrations of holes. This is most likely due to the crumpling and partial amorphization of the structure (Fig. S1, Supporting Material). GO-IL-Cl flakes are similar in structure to GO-IL-Ac, though they typically contain a higher concentration of defects (corrugations and holes). Additionally, a number of flakes appear to be somewhat fluffy and porous (Fig. 2c inset) revealing a high density of holes. SAED patterns exhibit similar graphitic rings to those in the previous samples ($d = 0.14$, 0.25 nm). However, it turns out that in more regions of this sample the rings are thicker and additional weak rings corresponding to 0.12 nm lattice parameter (due to the existence of a high density of defects that produce larger distortions of the graphitic lattice) are observed. The presence of wrinkles and holes, absent in non-irradiated material, suggests the laser-induced creation of structural defects in GO platelets, and a steady stress-induced bending of the GO sheets [39]. Moreover, the absence of diffraction spots corresponding to non-graphite structures suggests that the modified material does not form superlattice-like ordered assemblies.

Raman spectroscopy measurements allow additional insight into the structural configuration of the raw GO powder as well as the irradiated samples (Fig. 3a, Fig. S2a). The deconvolution of the spectra reveals dominating bands centred at around 1350 cm^{-1} (D) and 1590 cm^{-1} (G), besides the contribution of less intense and broader bands located at about 1200 cm^{-1} (I), 1500 cm^{-1} (D''), and 1680 cm^{-1} (D'). The G band is generated by the relative motion of sp^2 -bonded carbon atoms (E_{2g} phonon), whereas the D band is attributed to the breathing mode of six-fold rings and requires the presence of defects for its activation [40]. The D/G intensity ratio is frequently used as a figure of merit of the structural defect content of graphene materials. As observed in Table 1, D/G ratios of raw GO and GO-IL-Cl are very similar, 0.93 and 0.92 respectively, whereas the D/G value corresponding to GO-IL-Ac is somehow greater (0.97). D/G ratio of GO- H_2O sample (0.94) is also similar to that of Ref GO. The mean distance between defects (L_D), which can be also considered as the average graphitic domain size, and the density of structural defects (n_D) can be calculated from the D/G ratio [40,41]. Nevertheless, it is important to note that the calculation method depends on the degree of disorder in the GO platelets. Since FWHM of G band always increases with disorder, the plot of D/G versus FWHM(G) allows to discriminate the disorder regime of the studied material. Fig. 3b reveals that D/G ratio of Ref GO decreases with

Table 1

Average values of D/G, L_D , and n_D obtained from Raman spectra.

Sample	D/G	L_D (nm)	n_D (10^{13} cm^{-2})
Ref GO	0.93 ± 0.05	1.2 ± 0.3	2.27 ± 0.02
GO-IL-Ac	0.97 ± 0.02	1.2 ± 0.1	2.16 ± 0.01
GO-IL-Cl	0.92 ± 0.02	1.2 ± 0.2	2.30 ± 0.01
GO- H_2O	0.94 ± 0.03	1.2 ± 0.2	2.24 ± 0.01

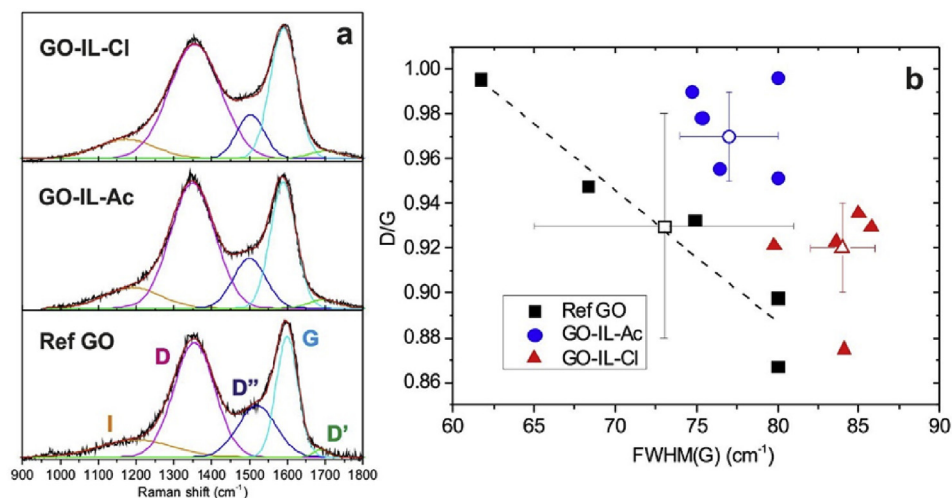


Fig. 3. (a) Typical Raman spectra obtained in reference GO, GO-IL-Ac and GO-IL-Cl samples, including the deconvoluted (I, D, D', G and G') bands. (b) D/G ratio as a function of the FWHM of G band obtained from all the spectra. The averaged values are depicted as open symbols. (A colour version of this figure can be viewed online.)

FWHM(G), i. e. disorder, pointing to a high defect density regime in which a large amount of defective carbon rings does not contribute to D band probably caused by their high distortion and opening. Since no evident structural defects are visible by TEM analyses, the most abundant defects would come from the sp^3 -bonded carbon-oxygen functionalities. The calculated L_D is quite small, about 1.2 nm, and the corresponding n_D is $2.27 \times 10^{13} \text{ cm}^{-2}$ (Table 1). Comparable results are witnessed in GO-H₂O sample (Fig. S2b, Table 1), pointing out to a similar structure than raw GO. As observed in Fig. 3b, the FWHM(G) obtained from GO-IL-Ac/Cl samples is concentrated at higher values accounting for larger structural disorder. As already stated, TEM study reveals that the irradiated GO sheets show high concentration of corrugations and holes, not observed in raw GO, accounting for their larger FWHM(G). Indeed, in accordance with the larger density of holes observed in GO-IL-Cl by TEM, GO-IL-Cl material reveals larger FWHM(G) values than GO-IL-Ac. However, no clear tendency of D/G versus FWHM(G) can be recognised in GO-IL-Ac and GO-IL-Cl, probably due to simultaneous and counteracting contributions of punctual defects and holes edges on the intensity of D and G bands [40,42]. As a consequence, the corresponding L_D and n_D values of these samples are very similar to those of Ref GO (Table 1). Nevertheless, these similar values do not represent similar structures, as TEM evidenced larger concentration of holes and wrinkles at irradiated samples (Fig. 2).

Compositional analysis is performed using XPS and FTIR. Representative high resolution XPS spectra of the investigated powders are presented in Fig. 4 and Fig. S3. C1s spectra are deconvoluted into four Gaussian peaks C1–C4, with maxima at 284.5, 286.2, 287.7, and 289.5 eV, respectively. These are ascribed to sp^2 carbon-carbon (C=C; C1) bonds (with some contribution from sp^3 C–C bonds), as well as epoxide-hydroxyl (C–O–C, C–OH; C2), carbonyl (C=O; C3) and carboxyl (COOH; C4) carbon-oxygen bonds [43]. O1s signals are also deconvoluted into four component peaks (O1–O4) sited at 531.3, 532.5, 533.7 and 534.9 eV. These peaks correspond to carbonyl (C=O; O1), sp^3 single bonded C–O (epoxy/phenolic; O2), carboxyl (O=C–O; O3) and chemisorbed water (O4) [44,45]. Interestingly, raw GO and GO-H₂O powders do not exhibit nitrogen component, although this element is clearly recorded in the irradiated GO-IL-Ac/Cl samples. N1s spectra acquired in GO-IL-Ac/Cl samples are deconvoluted into three components located at 398.5 eV (N1), 399.9 eV (N2) and 401.5 eV (N3). These peaks can be associated with pyridinic (N1), pyrrolic/amine (N2) and graphitic

(N3) carbon-nitrogen bonds [43]. It should be noted that pyridinic and pyrrolic N–C bonds will also contribute to the C2 and C3 peaks of the C1s spectrum (binding energies at 285.9 and 287.3 eV) [28,46], thus decreasing the relative contribution of hydroxyl–epoxide and carbonyl groups in these components. It is known that carbon atoms near to pyridinic nitrogens play a crucial role in oxidation–reduction reaction processes [47]. Moreover, rGO containing amino and amide species exhibit simultaneous p- and n-type semiconducting behaviour, enhancing the efficiency of the photocatalytic decomposition of water into H₂ and O₂ using visible wavelengths [23,26]. Finally, the Cl2p core-level spectrum of GO-IL-Cl sample was fitted by $2p_{3/2}$ – $2p_{1/2}$ spin-orbit doublets separated by 1.4 eV with an intensity ratio of 2:1. Accordingly, the spectrum can be deconvoluted into four components, denoted as Cl1–Cl4 and located at 200.2, 201.9, 197.6 and 198.9 eV, respectively (Fig. 4). These signals are attributed to two major components (Cl1 and Cl3) with their corresponding satellites at larger energies (Cl2, Cl4) [48]. The Cl1 signal could be ascribed to chlorine covalently bonded to carbon atoms, whereas Cl3 is attributed to chloride anions physisorbed on the graphene oxide platelets. It has to be noted that C–Cl bonds would also contribute to the C2 component of C1s spectrum [49,50].

Fig. 5 presents the C, O, and N atomic concentrations in the raw GO and irradiated powders, as well as the relative areas of the deconvoluted components in the high resolution C1s, O1s, and N1s spectra. The atomic concentrations, obtained from XPS wide scans, reveal that the concentration of carbon slightly increases after laser irradiation, from 77% to 83% in GO-IL-Ac/Cl samples. Conversely, a slight decrease is observed in GO-H₂O (73%). Moreover, a clear loss of oxygen atoms is observed (from 23% in Ref GO to 12% in GO-IL-Ac, and 11% in GO-IL-Cl), indicating that the raw GO has been partially reduced. In contrast, an increase of oxygen, up to 27%, is observed in GO-H₂O. Correspondingly, the reduction degree (C/O) increases from 3.4 in Ref GO to 7.1 and 7.7 in GO-IL-Ac and GO-IL-Cl, respectively, and decreases to 2.7 in GO-H₂O sample. Moreover, a clear incorporation of nitrogen is observed, with values approaching 5% in both GO-IL-Ac/Cl samples. The atomic concentration of chlorine in GO-IL-Cl is extremely low (0.2%) indicating that chlorine is essentially absent in the graphene structure. In summary, laser irradiation leads to the partial reduction and nitrogen doping of raw GO resulting in a modified GO structure with similar atomic concentrations in both IL solutions. Nevertheless, the relative areas of the deconvoluted components obtained via high resolution XPS

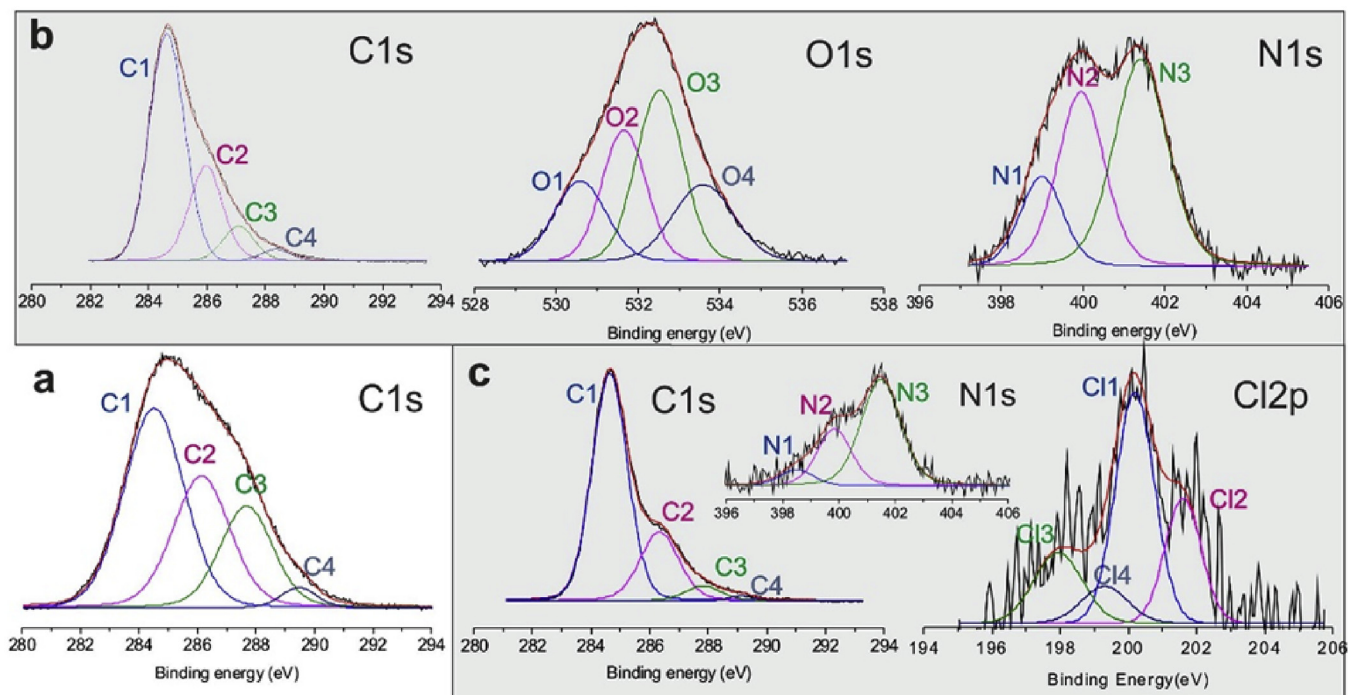


Fig. 4. Characteristic high resolution XPS spectra of (a) GO reference, (b) GO-IL-Ac and (c) GO-IL-Cl samples. The deconvoluted peaks of C1s, N1s, O1s and Cl2p signals are also included. (A colour version of this figure can be viewed online.)

reveal that the composition of the irradiated powder is slightly different in both cases. Raw GO is characterized by a relatively large quantity of sp^2 carbon and carbon bonded to oxygen species, without the presence of nitrogen-based groups. The higher areas correspond to the (C1, C2, O2, O3) components, indicating that,

besides graphitic domains, most of the carbon atoms form part of epoxy-phenolic and carboxylic functionalities. As previously stated, there is a loss of oxygen and a nitrogen inclusion in the GO structure after irradiation, leading to a very similar composition for both ILs. The resulting materials present decreased concentrations of epoxy

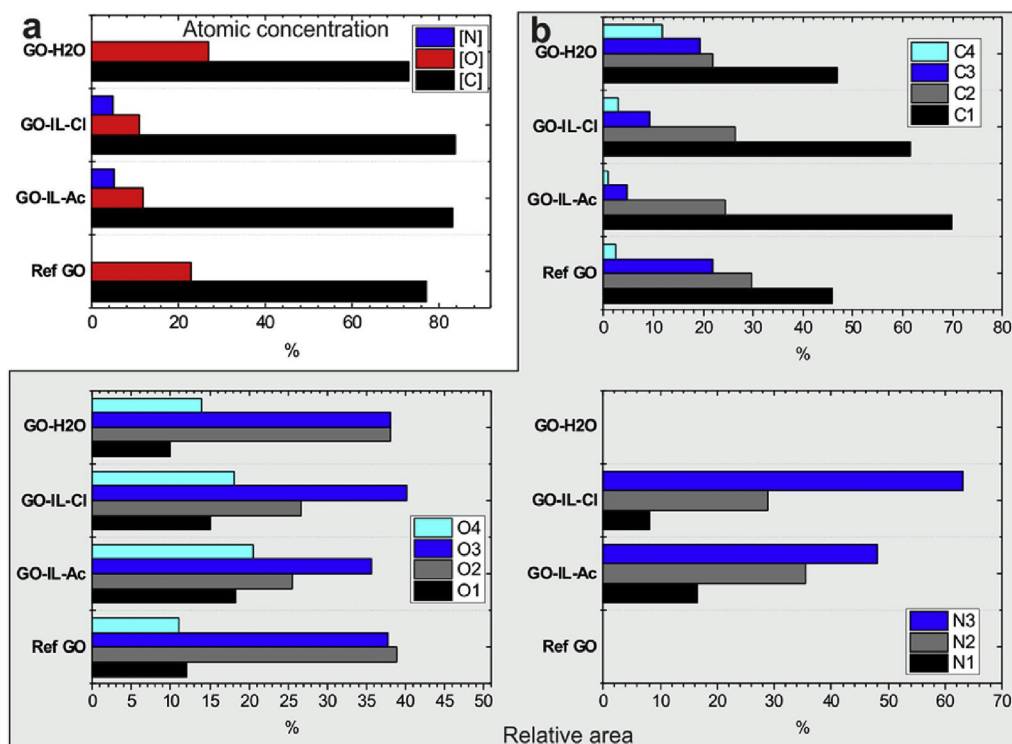


Fig. 5. (a) Atomic concentration and (b) relative areas of the deconvoluted components obtained in XPS analyses. (A colour version of this figure can be viewed online.)

- phenolic functionalities when compared to carboxylic and carbonyl groups (greater relevance of O3 in the O1s spectrum). As already indicated, pyridinic N–C bonds contribute to C2 peak (related to O2), leading to its increase when compared to C3–C4 components, despite the decrease in sp^3 carbon-oxygen bonds. Additionally, GO-IL-Cl presents a slightly larger relative content of carboxylic groups (C4, O3) than GO-IL-Ac. In terms of nitrogen functionalities, the most abundant in both cases is quaternary (graphitic) N, followed by pyrrolic and pyridinic nitrogen. Nevertheless, the ratio of graphitic versus pyrrolic – pyridinic groups is larger in GO-IL-Cl (63%) than in GO-IL-Ac (48%), whereas the percentage of pyridinic N is much larger in GO-IL-Ac (17%) than in GO-IL-Cl (8%). Accordingly, it is clear that the IL anion has an effective functionalization effect in the laser-induced doping process. In absence of IL molecules (GO-H₂O sample) the laser irradiation triggers totally different chemical reactions in GO flakes. As evidenced, oxygen incorporates in the GO structure mainly as carboxylic (C4, O3) and epoxy/phenolic (O2, C2) groups, leading to a more oxydized GO material.

The ATR-FTIR spectrum of raw GO presents representative peaks at 3369 cm^{-1} (–OH), 1720 cm^{-1} (C=O), 1623 cm^{-1} (C=C), 1220 cm^{-1} (C–O–C) and 1047 cm^{-1} (C–O) (Fig. 6) [51,52]. After irradiation of GO in the presence of both ionic liquids the spectra show a reduction of the C=O (1720 cm^{-1}) peaks, in accordance with XPS analyses (Fig. 4). Furthermore, two broad peaks at 3340 – 3359 and 1566 – 1578 cm^{-1} (assigned to –N–H bending) appear in both GO-IL-Ac and GO-IL-Cl spectra, confirming the N-doping of the GO platelets [52,53]. Interestingly, the appearance of the 1163 cm^{-1} peak could be attributed to the in-plane stretching of the imidazolium ring, confirming the initial interaction of the IL with the GO sheets, which is more pronounced for GO-IL-Ac [33]. Finally, the peak at 2950 cm^{-1} (attributed to CH₂ groups) suggests the presence of alkyl chains in the modified GO structure, most likely originating from [bmim] molecules.

¹H NMR spectra performed on the ILs prior to and after laser treatment, shown in Figs. S4 and S5, exhibit essentially the same peaks, indicating that no degradation of the supernatant ionic liquid occurs during irradiation. This result further confirms that radiation does not interact directly with the entities that form the bulk ILs (i.e. [bmim], Cl[–], CH₃COO[–]) leaving the material unchanged. Previous studies regarding the laser processing of GO in solid targets demonstrated that UV radiation is absorbed by GO flakes, inducing partial reduction by means of both photo-induced

chemical and thermal effects [16,20,43,54–56]. Conversely, it is known that imidazolium-based molecules are cationic and possess large electron affinities and π -conjugated orbitals [57]. As a result, such entities are prone to establish ion-exchange interactions with negatively charged GO sheets in addition to cation- π and π - π stacking with graphene domains [58,59]. Accordingly, it can be assumed that GO sheets dispersed in ILs are non-covalently bonded to a plethora of [bmim] molecules absorbed onto GO flakes [60]. Thus, the photolytic and photothermal mechanisms that GO flakes experience when exposed to laser radiation induce reaction of [bmim] with GO, which leads to the deoxygenation and nitrogen-doping of GO and the formation of N-rGO (Fig. 7). Interestingly, the anions of the ILs do not take part in the doping process, but do influence the proportion of chemical groups in N-rGO, most likely due to differences in the ionic strength. As a result, N-rGO synthesized using a IL-Cl solvent is similar in structure to IL-Ac but with a greater graphitic and reduced pyridinic-nitrogen content.

The photocatalytic activity of the prepared materials towards water splitting was tested using 0.25 M and 0.005 M solutions of methanol in water, as summarized in Fig. 8. The data obtained for the 0.25 M solution show an increasing concentration of hydrogen with time in almost all cases. It should be noted that the photocatalytic activity of the raw GO precursor is very low (with a measured gas concentration of $0.2\text{ }\mu\text{mol L}^{-1}$ at 210 min). GO-H₂O powder, which is slightly more oxidized and does not contain nitrogen functionalities, shows no photoactivity at all. However, GO-IL materials exhibit larger activity than raw GO (up to $1\text{ }\mu\text{mol L}^{-1}$ at 300 min), being GO-IL-Cl the material with the greater activity. In this regard, it should be noted that XPS investigations indicate that GO-IL-Cl materials contain a larger amount of graphitic nitrogen than GO-IL-Ac materials. Moreover, and conversely to pyridinic nitrogen, graphitic nitrogen has been proven to decrease the work function of graphene leading to n-type doping [61]. Accordingly, the combined p-n electronic nature of N-rGO (n-type component from graphitic N doping) and the interaction of graphitic nitrogen atoms with H⁺ can account for the enhanced photocatalytic efficiency for hydrogen evolution due to enhanced photogenerated charge separation and easier reduction of H⁺, respectively [22,62]. Furthermore, and in accordance with our results, Lavorato et al. showed that N-doped graphene catalysts increase water splitting efficiencies with the amount of graphitic N in its structure [63]. Consequently, it is anticipated that irradiation of GO-IL with different experimental conditions (leading to larger amount of graphitic N-doping) should result in enhanced photocatalysts. Alternatively, the obtained graphene-based materials could be also considered as metal-free co-catalysts. Accordingly, additional measurements were performed by mixing the obtained powders with identical amounts of anatase TiO₂ nanoparticles (20 nm average diameter) which act as the primary photocatalyst. Significantly, the amount of evolved hydrogen substantially increases (more than one order of magnitude) for GO-IL + TiO₂ catalysts when compared to GO-IL materials alone. Nevertheless, their activity is lower than the reference anatase TiO₂ nanoparticles. Therefore, it can be concluded that the GO-IL materials exhibit an adverse influence towards the TiO₂ activity, probably due to the scavenging of photons entering the reactor. Indeed, black GO-IL particles are also able to absorb the UVA photons used in photocatalytic experiments, thus leaving less photons available for TiO₂ photo-driven processes. It is worth noting that GO-H₂O + TiO₂ reveals no photogeneration of hydrogen at all (not shown). Therefore, the photoactivity of the GO-based materials seems to be effectively related to the nitrogen doping and the reduction degree of the GO structure.

Analogous investigations were performed using 0.005 M aqueous solutions of methanol, which are more comparable to working conditions in water splitting – photoreforming applications

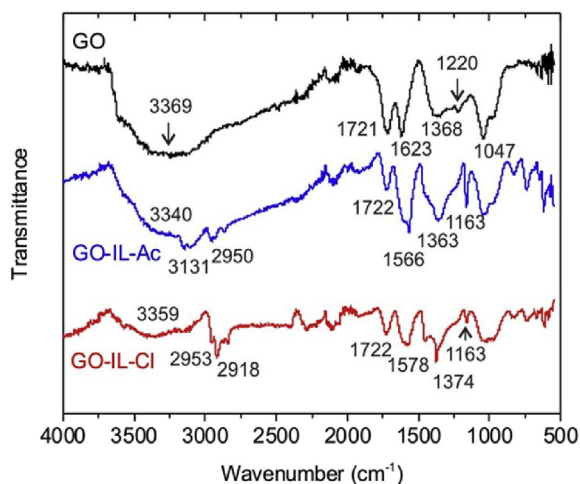


Fig. 6. ATR-FTIR spectra of reference GO (black), GO-IL-Ac (blue) and GO-IL-Cl (red) samples. (A colour version of this figure can be viewed online.)

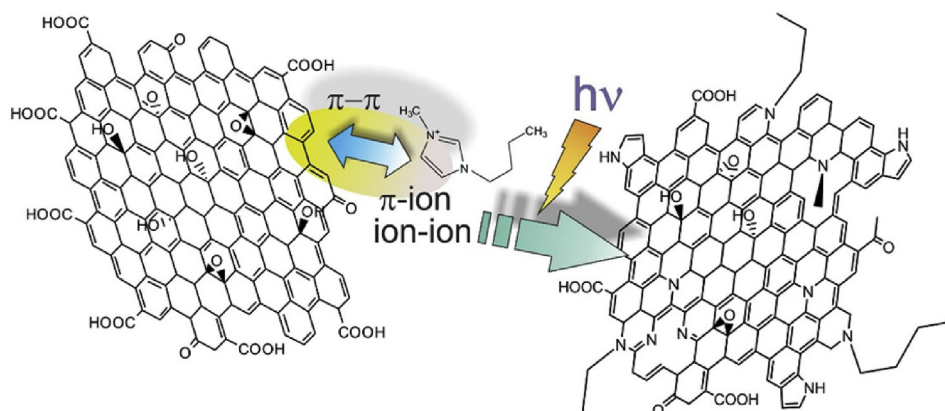


Fig. 7. Schematic illustration showing the interaction of GO with [bmim] molecules and the estimated chemical structure of the obtained N-rGO. (A colour version of this figure can be viewed online.)

(low concentrations of organic compounds, predictably diluted aqueous pollutants, as sacrificial agents). Alike to the results obtained with 0.25 M solution, GO-IL-Cl powder generates more hydrogen gas than GO-IL-Ac, although still less than the reference TiO_2 photocatalyst. Remarkably, the GO-IL-Ac + TiO_2 mixture leads to a much greater production of hydrogen gas than TiO_2 reference. The fact that GO-IL-Ac + TiO_2 mixture generates more hydrogen

than the separate contributions of GO-IL-Ac and TiO_2 confirms the synergistic effect between these materials.

As noted previously, equation (1) was used to quantify the photonic efficiencies of the prepared materials towards H_2 generation through photoreforming. Since the number of photons entering the reactor was $5.3 \times 10^{-7} \text{ E s}^{-1}$ and the productions of H_2 after 200 min of irradiation of the 0.25 M methanol slurries were (according to Fig. 8a) 0.26, 0.64, 0.42, 10.39, 51.5 and $89.29 \mu\text{mol L}^{-1}$ for GO, GO-IL-Ac, GO-IL-Cl, GO-IL-Ac + TiO_2 , GO-IL-Cl + TiO_2 and TiO_2 , respectively, the corresponding average photonic efficiencies, taking into account a reactor head space of 75 mL are 0.0006, 0.0015, 0.001, 0.024, 0.12 and 0.2%, respectively. Energy efficiencies calculated by considering an energy input into the reactor of $3.1 \times 10^{-3} \text{ W cm}^{-2}$ and a thermochemical energy associated with the H-H bond of $283.6 \text{ kJ mol}^{-1}$ are 0.0003, 0.00075, 0.0005, 0.012, 0.06 and 0.1% for GO, GO-IL-Ac, GO-IL-Cl, GO-IL-Ac + TiO_2 , GO-IL-Cl + TiO_2 and TiO_2 , respectively. With the 0.005 M ethanol slurries the production of H_2 was lower and, consequently, the photonic and the energy efficiencies were also lower. Nevertheless, it is interesting to remark that efficiencies obtained with the GO-IL-Ac + TiO_2 mixture after 250 min of irradiation (0.008% photonic efficiency and 0.004% energy efficiency) are much larger than the ones for TiO_2 after the same irradiation time (0.0016% photonic efficiency and 0.0008% energy efficiency). Since H_2 production with naked TiO_2 photo-reforming is considered to be discrete, it is concluded that H_2 concentrations are low. Nevertheless, the synergy between GO-IL-Ac and TiO_2 when using low concentrations of the organic sacrificial agent leaves the door open for a further exploration of the photocatalytic potential of those materials.

It is known that the surface of metal oxides exposed to water becomes hydroxylated, and in this respect titanium dioxide is no exception [64]. As a result, pyridine functionalities of dispersed N-rGO sheets can form hydrogen bonds with hydroxyl groups present on the nanoparticle surface [65]. Furthermore, direct Ti–pyridinic nitrogen coordination bonds can be formed by the donor-acceptor interaction of unsaturated Ti^{+n} ions at the TiO_2 surface and dative pyridine nitrogen atoms [65,66]. Moreover, previous studies indicate that a strong pyridine-Ti coordination bond is likely to lead to the formation of efficient electron conduction pathways [67,68] which, in our case, are likely to enhance the photogenerated charge-transfer processes between N-rGO and TiO_2 , leading to more efficient hydrogen generation. This effect would be more extensive in GO-IL-Ac than in GO-IL-Cl since the former contains a higher proportion of pyridine-like nitrogen groups (obtained in the experiments performed with 0.005 M methanol solution). However, excessive concentration of methanol (e.g. 0.25 M) would lead

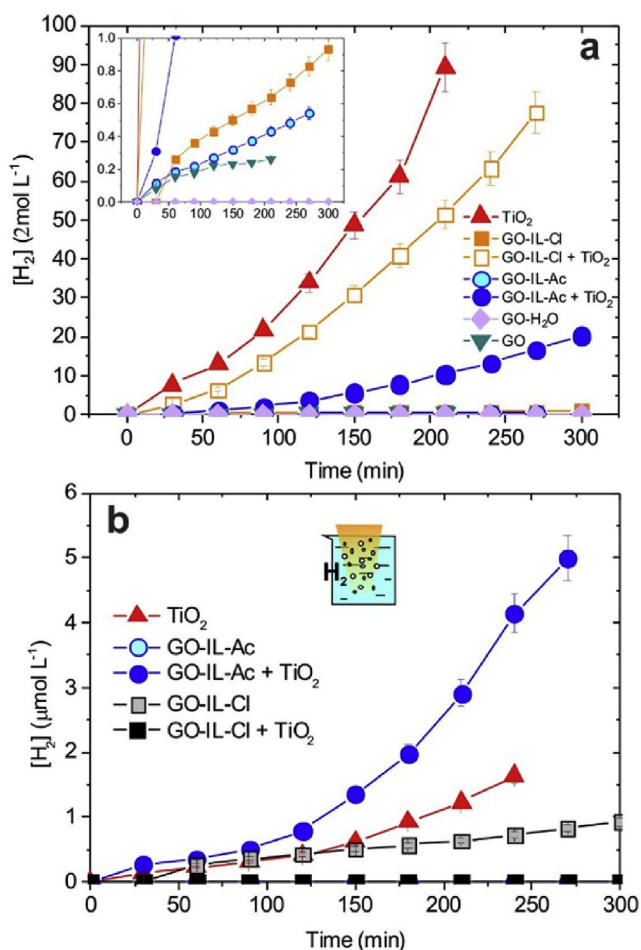


Fig. 8. Generated hydrogen evolution with time in (a) 0.25 M and (b) 0.005 M methanol aqueous solutions. Inset in 0.25 M: zoom at low concentration hydrogen range. (A colour version of this figure can be viewed online.)

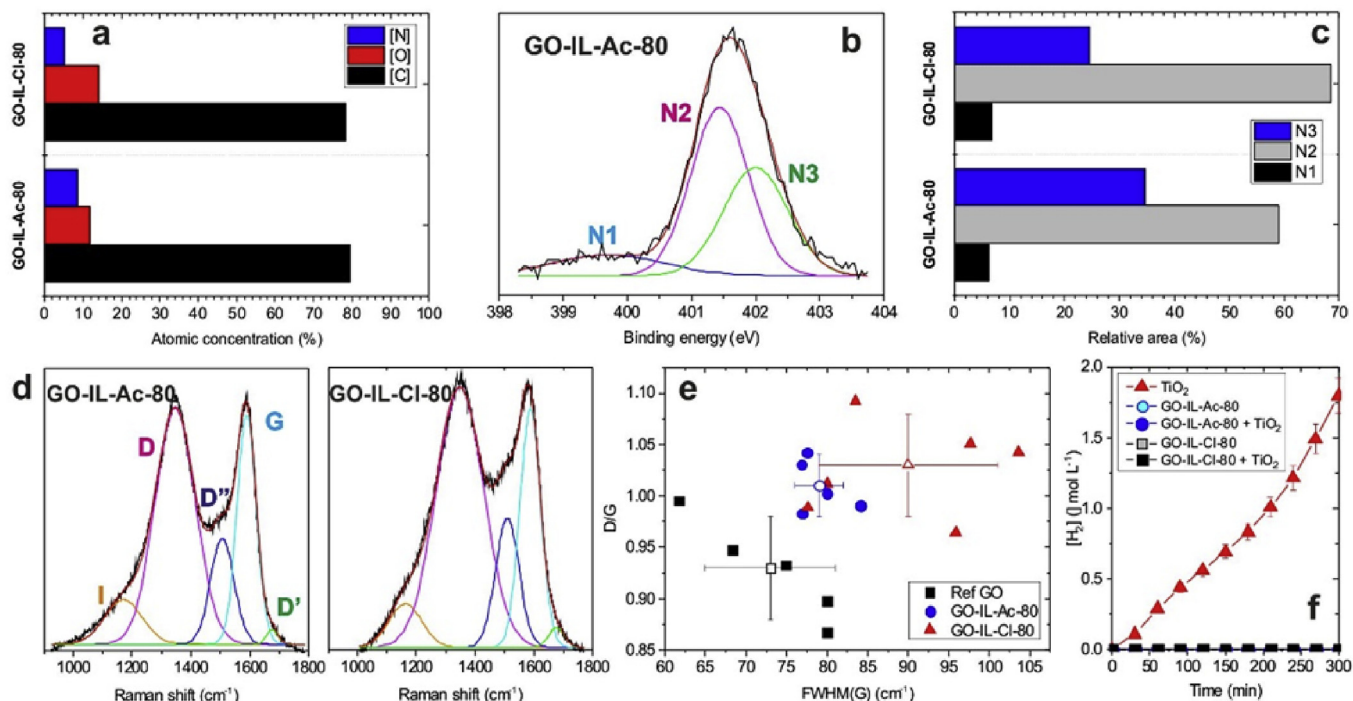


Fig. 9. Study of samples GO-IL-Ac-80 and GO-IL-Cl-80. (a) XPS atomic concentration. (b) N1s high resolution XPS spectrum of GO-IL-Ac-80. (c) Relative areas of the N1s deconvoluted components. (d) Representative Raman spectra of the samples. (e) D/G ratio as a function of the FWHM(G) from all the Raman spectra. The averaged values are depicted as open symbols. (f) Generated hydrogen evolution with time in 0.005 M methanol aqueous solution. (A colour version of this figure can be viewed online.)

to the adsorption of methanol molecules on the TiO_2 surface [69]. Consequently, adsorbed methanol molecules would impede the formation of Ti-pyridinic N bonds and corresponding conduction pathways, leading to a decrease in photocatalytic efficiency.

Further experiments were conducted using dispersions of 1 wt.% of GO powder in aqueous solutions containing higher concentrations, ca. 80 wt.%, of [bmim]Ac and [bmim]Cl, respectively named as GO-IL-Ac-80 and GO-IL-Cl-80. Our aim was to increase the N-doping of GO and to confirm the role of the nitrogen containing groups on the hydrogen generation rate. After laser irradiation, filtering and drying in identical experimental conditions as in the case of the GO-IL-Ac and GO-IL-Cl samples, the structure and composition of the powder materials were studied. As observed in Fig. 9a, atomic concentration obtained through wide scan XPS reveals a carbon content of 80% and 78% for GO-IL-Ac-80 and GO-IL-Cl-80, respectively. Besides, their oxygen concentration are 12% and 14%, leading to a reduction degree (C/O) of 6.7 and 5.6 in GO-IL-Ac-80 and GO-IL-Cl-80, respectively. These C/O values are lower than the corresponding ones of their low IL concentration counterparts (GO-IL-Ac/Cl), what accounts for a somehow less efficient reduction process. However, larger incorporation of nitrogen is observed in GO-IL-Ac-80 (8.6%) as compared to GO-IL-Cl-80 (5%) which remains comparable to those of GO-IL-Ac/Cl samples. The atomic concentration of Cl in GO-IL-Cl-80 is about 2.5%. Fig. S6 shows the high resolution XPS spectra of both materials. Interestingly, the high resolution N1s spectra reveal different components configuration as compared to GO-IL-Ac/Cl (Fig. 9b and c). As observed, the largest contribution corresponds to pyrrolic/amine functionalities (N2) with ca. 60%/70% contribution, followed by graphitic (N3; 35%/25%) and pyridinic (N1; 6.3%/6.8%) groups in GO-IL-Ac-80 and GO-IL-Cl-80, respectively. It is worth reminding that the amount of graphitic and pyridinic groups are significantly larger in GO-IL-Ac/Cl materials. Raman spectroscopy of GO-IL-Ac-80 and GO-IL-Cl-80 reveals similar spectra to those of GO-IL-Ac/Cl (Fig. 9d). Their corresponding (D/G , L_D , n_D) values are

(1.01 ± 0.03 , 1.2 ± 0.1 nm, $(2.09 \pm 0.09) \times 10^{13}$ cm $^{-2}$) and (1.03 ± 0.05 , 1.3 ± 0.3 nm, $(2.06 \pm 0.02) \times 10^{13}$ cm $^{-2}$). These values are also very similar to those corresponding to GO-IL-Ac/Cl materials. Besides, FWHM(G) values are also greater than those of raw GO, what stands for larger structural disorder (Fig. 9e).

The photocatalytic activity of GO-IL-Ac-80 and GO-IL-Cl-80 materials was also studied and compared to previous water splitting experiments performed with GO-IL-Ac/Cl samples. Fig. 9f shows the evolution with time of the generated hydrogen in 0.005 M methanol aqueous solutions. As observed, the generation of hydrogen by GO-IL-Ac-80, GO-IL-Cl-80, GO-IL-Ac-80 + TiO_2 , GO-IL-Cl-80 + TiO_2 is negligible as compared to reference TiO_2 and GO-IL-Ac/Cl materials. It is important to remind that the quantity of nitrogen in the structure of GO-IL-Ac-80 (8.6%) is higher than in GO-IL-Ac/Cl and GO-IL-Cl-80 materials (5%). Therefore, it appears clear that the total amount of nitrogen is not the key parameter for the photocatalytic efficiency. Most of the nitrogen functionalities in GO-IL-Ac/Cl-80 are pyrrolic, whereas in GO-IL-Ac/Cl are graphitic-pyridinic. Consequently, the photocatalytic results support the hypothesis that the presence of graphitic-pyridinic groups are crucial for the enhancement of photoactivity of the graphene derivatives. On the other hand, the laser-induced chemical paths have revealed to be complex since the increase of IL concentration in GO dispersions led to the formation of pyrrolic versus graphitic-pyridinic nitrogen species, which resulted to be counter-productive. Therefore, new strategies should be explored for the development of graphene materials with higher amount of graphitic-pyridinic functionalities for increasing photocatalytic efficiency.

4. Conclusion

The results presented herein demonstrate that UV laser irradiation of GO dispersions in [bmim] ionic liquids (using chloride and acetate anions) is an effective, fast and simple route for obtaining

N-doped rGO powder. Neither vacuum or annealing processes are required, and the basic technique can be easily scaled to an environmentally friendly and non-toxic industrial environment. Significantly, results illustrate that the photoactivity is mainly linked to N-doping and reduction degree of GO. Besides the IL concentration, a change in the anion type in the ionic liquid can yield different graphitic-pyridinic-pyrrolic-nitrogen ratios, which lead to very different photocatalytic performances. N-rGO powder obtained with low concentration [bmim]Cl IL exhibits higher proportions of quaternary N and higher photoactivity functioning as photocatalyst when compared to that synthesized with [bmim]Ac IL. Conversely, the latter exhibits greater ratio of pyridinic-N and a remarkable synergistic activity acting as co-catalyst with anatase nanoparticles. High IL concentration dispersions lead to the formation of pyrrolic-rich graphene derivatives which show no photoactivity. The interplay between the graphene-based photocatalyst, water, methanol and TiO₂ nanoparticles has revealed very rich phenomenology which requires further investigation.

Acknowledgements

The authors thank the financial support of the Spanish Ministry of Economy, Industry and Competitiveness under the projects ENE2014-56109-C3-3-R and HIDROPILSOL (CTQ2013-47103-R), in addition to the MAT2016-77852-C2-1-R (AEI/FEDER, UE). JPL acknowledges funding from the Swiss National Science Foundation (the project no. 200021_160174) and the EU (ERC-2015-STG microCrysFact 677020). SG thanks to MINECO for a FPI predoctoral grant and the project TEC2014-51940-C2-2 (EU ERDF, FEDER). ICMA acknowledges financial support from the Spanish Ministry of Economy, Industry and Competitiveness, through the “Severo Ochoa” Programme for Centres of Excellence in R&D (SEV-2015-0496). The authors also thank Dr. Nuria Aliaga and Ms. Wenjie Qian for their assistance in centrifugation and separation processes.

Appendix A. Supplementary data

Supplementary data related to this article can be found at <https://doi.org/10.1016/j.carbon.2017.12.116>.

References

- [1] G. Zhang, X. Wan, A wind-hydrogen energy storage system model for massive wind energy curtailment, *Int. J. Hydrogen Energy* 39 (3) (2014) 1243–1252.
- [2] K. Maeda, Photocatalytic water splitting using semiconductor particles: history and recent developments, *J. Photochem. Photobiol. C Photochem. Rev.* 12 (4) (2011) 237–268.
- [3] K. Villa, et al., Heterogeneous photocatalytic hydrogen generation in a solar pilot plant, *Int. J. Hydrogen Energy* 38 (29) (2013) 12718–12724.
- [4] A. Patsoura, D.I. Kondarides, X.E. Verykios, Photocatalytic degradation of organic pollutants with simultaneous production of hydrogen, *Catal. Today* 124 (3–4) (2007) 94–102.
- [5] W. Fan, et al., Nanocomposites of TiO₂ and reduced graphene oxide as efficient photocatalysts for hydrogen evolution, *J. Phys. Colloid Chem.* 115 (21) (2011) 10694–10701.
- [6] M. Ni, et al., A review and recent developments in photocatalytic water-splitting using TiO₂ for hydrogen production, *Renew. Sustain. Energy Rev.* 11 (3) (2007) 401–425.
- [7] K. Villa, et al., Nitrogen doped TiO₂ for hydrogen production under visible light irradiation, *Sol. Energy* 86 (1) (2012) 558–566.
- [8] K. Sivula, Metal oxide photoelectrodes for solar fuel production, surface traps, and catalysis, *J. Phys. Chem. Lett.* 4 (10) (2013) 1624–1633.
- [9] J. Ran, et al., Earth-abundant cocatalysts for semiconductor-based photocatalytic water splitting, *Chem. Soc. Rev.* 43 (22) (2014) 7787–7812.
- [10] A.C. Ferrari, et al., Science and technology roadmap for graphene, related two-dimensional crystals, and hybrid systems, *Nanoscale* 7 (11) (2015) 4598–4810.
- [11] Q. Xiang, J. Yu, Graphene-based photocatalysts for hydrogen generation, *Journal of Physical Chemistry Letters* 4 (5) (2013) 753–759.
- [12] D.R. Dreyer, et al., The chemistry of graphene oxide, *Chem. Soc. Rev.* 39 (1) (2010) 228–240.
- [13] L. Huang, et al., Pulsed laser assisted reduction of graphene oxide, *Carbon* 49 (7) (2011) 2431–2436.
- [14] L.M. Cao, et al., Synthesis of diamond from carbon nanotubes under high pressure and high temperature, *Carbon* 39 (2) (2001) 311–314.
- [15] P. Kumar, et al., Novel radiation-induced properties of graphene and related materials, *Macromol. Chem. Phys.* 213 (10–11) (2012) 1146–1163.
- [16] A. Perez del Pino, et al., Study of the deposition of graphene oxide by matrix-assisted pulsed laser evaporation, *J. Phys. Appl. Phys.* 46 (50) (2013).
- [17] M. Koinuma, et al., Photochemical engineering of graphene oxide nanosheets, *J. Phys. Colloid Chem.* 116 (37) (2012) 19822–19827.
- [18] W.H. Lee, et al., Selective-area fluorination of graphene with fluoropolymer and laser irradiation, *Nano Lett.* 12 (5) (2012) 2374–2378.
- [19] M. Kim, et al., Light-driven reversible modulation of doping in graphene, *Nano Lett.* 12 (1) (2012) 182–187.
- [20] A.P. del Pino, et al., Laser-induced chemical transformation of free-standing graphene oxide membranes in liquid and gas ammonia environments, *Rsc Advances* 6 (55) (2016) 50034–50042.
- [21] S. Moussa, et al., Pd-partially reduced graphene oxide catalysts (Pd/PRGO): laser synthesis of Pd nanoparticles supported on PRGO nanosheets for carbon-carbon cross coupling reactions, *ACS Catal.* 2 (1) (2012) 145–154.
- [22] T.-F. Yeh, et al., Roles of graphene oxide in photocatalytic water splitting, *Mater. Today* 16 (3) (2013) 78–84.
- [23] T.-F. Yeh, et al., Tuning the electronic structure of graphite oxide through ammonia treatment for photocatalytic generation of H₂ and O₂ from water splitting, *J. Phys. Colloid Chem.* 117 (13) (2013) 6516–6524.
- [24] X. Wang, et al., N-doping of graphene through electrothermal reactions with ammonia, *Science* 324 (5928) (2009) 768–771.
- [25] Y. Li, et al., Nitrogen-doped graphene quantum dots with oxygen-rich functional groups, *J. Am. Chem. Soc.* 134 (1) (2012) 15–18.
- [26] T.-F. Yeh, et al., Nitrogen-doped graphene oxide quantum dots as photocatalysts for overall water-splitting under visible light illumination, *Adv. Mater.* 26 (20) (2014), p. 3297–.
- [27] J.R. Potts, et al., Graphene-based polymer nanocomposites, *Polymer* 52 (1) (2011) 5–25.
- [28] D. Kepic, et al., Nanosecond laser-assisted nitrogen doping of graphene oxide dispersions, *ChemPhysChem* 18 (2017) 935–941.
- [29] R.D. Rogers, K.R. Seddon, Ionic liquids – solvents of the future? *Science* 302 (5646) (2003) 792–793.
- [30] J.G. Huddleston, et al., Characterization and comparison of hydrophilic and hydrophobic room temperature ionic liquids incorporating the imidazolium cation, *Green Chem.* 3 (4) (2001) 156–164.
- [31] M. Armand, et al., Ionic-liquid materials for the electrochemical challenges of the future, *Nat. Mater.* 8 (8) (2009) 621–629.
- [32] N.V. Plechkova, K.R. Seddon, Applications of ionic liquids in the chemical industry, *Chem. Soc. Rev.* 37 (1) (2008) 123–150.
- [33] P. Bhunia, et al., Synthesis of highly n-type graphene by using an ionic liquid, *Chemistry-a European Journal* 18 (39) (2012) 12207–12212.
- [34] P. Bhunia, et al., A non-volatile memory device consisting of graphene oxide covalently functionalized with ionic liquid, *Chem. Commun.* 48 (6) (2012) 913–915.
- [35] J.-Y. Liu, et al., Synthesis of nitrogen-doped graphene by pyrolysis of ionic-liquid-functionalized graphene, *J. Mater. Chem. C* 1 (9) (2013) 1713–1716.
- [36] J.L. Anderson, et al., Characterizing ionic liquids on the basis of multiple solvation interactions, *J. Am. Chem. Soc.* 124 (47) (2002) 14247–14254.
- [37] A.M. Braun, M.T.M.E. Oliveros, *Photochemical Technology*, Wiley, New York, 1991.
- [38] N.R. Wilson, et al., Graphene oxide: structural analysis and application as a highly transparent support for electron microscopy, *ACS Nano* 3 (9) (2009) 2547–2556.
- [39] Z. Qin, et al., Effect of wrinkles on the surface area of graphene: toward the design of nanoelectronics, *Nano Lett.* 14 (11) (2014) 6520–6525.
- [40] A.C. Ferrari, D.M. Basko, Raman spectroscopy as a versatile tool for studying the properties of graphene, *Nat. Nanotechnol.* 8 (4) (2013) 235–246.
- [41] L.G. Cancado, et al., Quantifying defects in graphene via Raman spectroscopy at different excitation energies, *Nano Lett.* 11 (8) (2011) 3190–3196.
- [42] M.M. Lucchese, et al., Quantifying ion-induced defects and Raman relaxation length in graphene, *Carbon* 48 (5) (2010) 1592–1597.
- [43] A. Perez del Pino, et al., Laser-induced chemical transformation of graphene oxide-iron oxide nanoparticles composites deposited on polymer substrates, *Carbon* 93 (2015) 373–383.
- [44] S. Benkoulal, et al., Water adsorption on TiO₂ surfaces probed by soft X-ray spectroscopies: bulk materials vs. isolated nanoparticles, *Sci. Rep.* (2015) 5.
- [45] Z. Xing, et al., One-pot hydrothermal synthesis of Nitrogen-doped graphene as high-performance anode materials for lithium ion batteries, *Sci. Rep.* (2016) 6.
- [46] T.I.T. Okpalugo, et al., High resolution XPS characterization of chemical functionalised MWCNTs and SWCNTs, *Carbon* 43 (1) (2005) 153–161.
- [47] T. Xing, et al., Observation of active sites for oxygen reduction reaction on nitrogen-doped multilayer graphene, *ACS Nano* 8 (7) (2014) 6856–6862.
- [48] E.T. Kang, H.C. Ti, K.G. Neoh, Xps studies of some chemically synthesized polypyrrole organic acceptor complexes, *Polym. J.* 20 (10) (1988) 845–850.
- [49] J. Hubert, et al., Plasma polymerization of C₄Cl₆ and C₂H₂Cl₄ at atmospheric pressure, *Polymer* 54 (16) (2013) 4085–4092.
- [50] J. Zheng, et al., Production of graphite chloride and bromide using microwave sparks, *Sci. Rep.* (2012) 2.
- [51] M. Khandelwal, A. Kumar, One-pot environmentally friendly amino acid mediated synthesis of N-doped graphene-silver nanocomposites with an enhanced multifunctional behavior, *Dalton Trans.* 45 (12) (2016) 5180–5195.

- [52] J. Jang, et al., Effects of the alkylamine functionalization of graphene oxide on the properties of polystyrene nanocomposites, *Nanoscale Res. Lett.* (2014) 9.
- [53] M.J. Ju, et al., N-doped graphene nanoplatelets as superior metal-free counter electrodes for organic dye-sensitized solar cells, *Acs Nano* 7 (6) (2013) 5243–5250.
- [54] E. Gyoergy, et al., Effect of nitrogen doping on wetting and photoactive properties of laser processed zinc oxide-graphene oxide nanocomposite layers, *J. Appl. Phys.* 116 (2) (2014).
- [55] S.M. O'Malley, et al., Resonant infrared and ultraviolet matrix-assisted pulsed laser evaporation of titanium oxide/graphene oxide composites: a comparative study, *J. Phys. Colloid Chem.* 118 (48) (2014) 27911–27919.
- [56] A. Datcu, et al., One-step preparation of nitrogen doped titanium oxide/Au/reduced graphene oxide composite thin films for photocatalytic applications, *Rsc Advances* 5 (61) (2015) 49771–49779.
- [57] C.M. Maroneze, et al., Electroactive properties of 1-propyl-3-methylimidazolium ionic liquid covalently bonded on mesoporous silica surface: development of an electrochemical sensor probed for NADH, dopamine and uric acid detection, *Electrochim. Acta* 123 (2014) 435–440.
- [58] R. Bari, et al., Direct exfoliation of graphene in ionic liquids with aromatic groups, *Colloid. Surface. Physicochem. Eng. Aspect.* 463 (2014) 63–69.
- [59] Y.-K. Yang, et al., Non-covalently modified graphene sheets by imidazolium ionic liquids for multifunctional polymer nanocomposites, *J. Mater. Chem.* 22 (12) (2012) 5666–5675.
- [60] L. Tian, et al., The adsorption of water-soluble ionic liquids on graphene oxide of different oxygen content, *Rsc Advances* 4 (102) (2014) 58536–58545.
- [61] T. Schiros, et al., Connecting dopant bond type with electronic structure in N-Doped graphene, *Nano Lett.* 12 (8) (2012) 4025–4031.
- [62] F. Pei, et al., Effective improvement of photocatalytic hydrogen evolution via a facile in-situ solvothermal N-doping strategy in N-TiO₂/N-graphene nanocomposite, *Int. J. Hydrogen Energy* 39 (13) (2014) 6845–6852.
- [63] C. Lavorato, et al., N-doped graphene derived from biomass as a visible-light photocatalyst for hydrogen generation from water/methanol mixtures, *Chem. Eur J.* 20 (1) (2014) 187–194.
- [64] H. Hussain, et al., Structure of a model TiO₂ photocatalytic interface, *Nat. Mater.* 16 (4) (2017), p. 461–+.
- [65] T. Bezrodna, et al., Pyridine-TiO₂ surface interaction as a probe for surface active centers analysis, *Appl. Surf. Sci.* 214 (1–4) (2003) 222–231.
- [66] P. Jones, J.A. Hockey, Infra-red studies of rutile surfaces .1, *Trans. Faraday Soc.* 67 (585) (1971), p. 2669-&.
- [67] G.D.P. Koujiro Tambara, Supramolecular chemistry of donor–acceptor interactions, *Annu. Rep. Prog. Chem. Sect. B: Org. Chem.* 108 (2012) 186–201.
- [68] Y. Ooyama, et al., Dye-sensitized solar cells based on donor-pi-acceptor fluorescent dyes with a pyridine ring as an electron-withdrawing-injecting anchoring group, *Chemistry-a European Journal* 17 (52) (2011) 14837–14843.
- [69] X. Lang, et al., Interplay between methanol and anatase TiO₂(101) surface: the effect of subsurface oxygen vacancy, *J. Phys. Colloid Chem.* 121 (11) (2017) 6072–6080.